JOURNAL OF AEROSPACE INFORMATION SYSTEMS
Vol. 17, No. 12, December 2020

Mitigation of Ground Impact Hazard for Safe Unmanned Aerial Vehicle Operations

Andrew Poissant,* Lina Castano,† and Huan Xu‡
University of Maryland, College Park, Maryland 20742

https://doi.org/10.2514/1.I010797

Autonomous operation of unmanned aerial vehicles (UAVs) requires development of technologies that allow for safer flight control and response to various flight anomalies. Software for autonomous control should allow the UAV to detect and avoid potential hazards, as well as respond to critical failures midflight without input from a human operator. This paper develops a ground impact and hazard mitigation (GIHM) module that integrates the following: 1) consideration of engine and control surface failure flight modes, 2) generation of feasible ground impact footprints based on glide equations, 3) selection of safest response ground impact sites based on a high-resolution LandScan USA population dataset, and 4) controlled descent to a selected site. For a sample population distribution, integration of GIHM with standard UAV flight software shows a maximum casualty expectation reduction of 97% compared to the flight software without GIHM near highly populated areas. Incorporation of this hazard mitigation module is successful in reducing fatalities per flight hour, bringing UAVs closer to being safe enough for integration into the National Airspace System.

Nomenclature

A_r	=	wing aspect ratio
C_D	=	coefficient of drag
C_{do}	=	profile drag
C_L	=	coefficient of lift
C_{L_α}	=	angle-of-attack stability derivative
C_{L_0}	=	coefficient of lift at zero angle of attack
D	=	drag
D_{glide}	=	glide distance during straight level phase
$d\psi$	=	total change in heading
d_x	=	total distance traveled in x direction during gliding flight
$d_{x,s}$	=	distance traveled in x direction during straight level phase
$d_{x,t}$	=	distance traveled in x direction during turning phase
d_y	=	total distance traveled in y direction during gliding flight
$d_{y,s}$	=	distance traveled in y direction during straight level phase
$d_{y,t}$	=	distance traveled in y direction during turning phase
g	=	acceleration of gravity
h_i	=	aircraft's initial height before entering gliding flight
k	=	induced drag factor
L	=	lift
L_{arc}	=	arclength of circle made by a turn
m	=	aircraft mass
R	=	radius of the circle during the turning phase
S	=	wing area
T	=	thrust
v	=	airspeed
v_s	=	sink rate
W	=	aircraft weight
α	=	angle of attack
Δh_{turn}	=	height loss during the turning phase
θ	=	pitch angle
ρ_0	=	density of air at sea level
ϕ	=	roll angle
ψ	=	yaw angle
$\dot{\psi}$	=	turn rate

Received 9 September 2019; revision received 21 July 2020; accepted for publication 23 July 2020; published online 7 September 2020.

*Graduate Research Assistant, Institute for Systems Research. Member AIAA.

†Assistant Research Scientist, Department of Aerospace Engineering. Member AIAA.

‡Assistant Professor, Department of Aerospace Engineering. Member AIAA.

I. Introduction

SOFTWARE for the control of unmanned aerial vehicles (UAVs) has become increasingly sophisticated and elaborate over the past decade. The main focus on such software, however, has been on automatic control: not autonomous control [1]. Automatic control provides the necessary automation of nominal operational control, whereas autonomous control must allow for a level of autonomy that predicts and responds to any event and condition [1]. There remains a critical need for fully developed safety software within the UAV system architecture that can make informed decisions in the presence of flight anomalies [2]. This work presents a decision-making module that is able to respond to critical flight anomalies and minimize hazards to other aircraft and the general population.

Major hazards associated with UAV operations include collisions between the UAV and other aircraft, as well as impact of the UAV with terrain, people, or structures [3]. These hazards pose a large risk to the general public, with casualties being a worst-case scenario. UAVs can have accident rates as high as 32 accidents per 100,000 flight hours: 32 times higher than the accident rates for small general aviation aircraft, and 3200 times higher than large airliners [2]. With UAV accident rates significantly higher than that of conventionally piloted aircraft, there is a clear need for additional safety measures for UAV control software and hardware before they can be integrated into the National Airspace System (NAS).

A 2012 congressional report detailed the required technology and standard procedures for safe UAV operations [4], requiring UAVs to sense and avoid other air traffic under all possible scenarios, including loss of communications. Also, the UAV must be able to autonomously return home or determine a safe path to a crashing location [4]. Furthermore, as detailed in Ref. [5], all UAVs must operate in restricted airspace or at extremely low altitudes, which increases the risk of collision. To integrate UAVs into the NAS, airborne safety must be ensured by avoiding midair collisions and guarding against ground impact in the event of an impending crash. The contribution of this paper is the development of a module that guards against casualties due to ground impact and its integration with flight software. This module focuses on the effects of critical vehicle failure modes and the vehicle's ability to reach a safe crash location.

Characterizing failure modes is an important aspect in guarding against ground impact. The failure mode determines the capabilities and maneuverability of the aircraft, which must be considered when developing ground footprint models in order to reduce its hazard on the ground. For UAVs, modes may include actuator and sensor failures, engine malfunction, loss of radio link and Global Positioning System (GPS), as well as structural damage such as a broken propeller, wing, etc., caused by unanticipated flight events [6]. This paper focuses on two particular categories: engine malfunction and actuator failures. We investigate engine malfunctions because of their prevalence as one of the root causes of Unmanned aerial systems (UAS) failures [7]. Actuator faults are studied because they contain several moving parts and are among the least reliable components on a UAV. Because actuators are connected to aerodynamic control surfaces, actuator faults directly affect the flight dynamics of the UAV. Actuator failures can lead to significant loss in controllability of the aircraft and, eventually, catastrophic failure [8].

A wide body of literature exists in assessing the collective risk that faulty UAVs pose, both in air [2,9,10] and on the ground [9–14]. In particular, ground risk models have the following general components: failure mode, impact location, recovery, stress, exposure, incident stress, and harm [15]. Of these components, our work entails the following: failure modes, ground impact location, stress caused by fatalities, and exposure via population data. Previous works have developed impact location models such as ground footprints and geometries of reachable areas [15]. The work presented in Ref. [16] investigated the ability of a fixed-wing aircraft to glide to a designated emergency landing area. The authors in Refs. [3,17] use six-degree-of-freedom (6-DOF) models to develop ground impact models for determining the reachable ground envelope of UAVs. Research in Ref. [18] developed an emergency flight planning architecture where footprint generation initiates a multiobjective landing site selection process, which includes consideration of winds, runway feasibility, aircraft states, and waypoint generation. None of these works, however, incorporate flight control software into these models. They furthermore do not examine collective risk profiles that consider high-resolution population data and reaction protocols for real-time implementation, as our work does.

Accurate population data can be used to further understand the collective risk a UAV poses to a given area. Previous work has used census data or local tax data [9–13]. Research in Ref. [19] uses census data in addition to mobile phone activity for real-time occupancy estimation, where both census and phone data are statistically analyzed and fused for risk-aware flight planning decisions. Mobile phone and traffic data are not easy to access today, and yet they may be easy to access in the future. In addition, census data alone can be largely unrepresentative of the true population count for a given area. The work of Ref. [20] used demographic population data for entire cities and states to generate population data for use in developing collective risk profiles. Using data at such large scales can result in significant uncertainty if finer-resolution population data are required. For this reason, population data based on LandScan USA data were used in our work to obtain accurate population data.

LandScan is a high-resolution population distribution database that provides spatial and temporal information. It uses best available demographic (census data) and geographic data, as well as remote sensing imagery analysis techniques, and applies multivariate dasymetric modeling [21] to disaggregate census counts within an administrative boundary. Dasymetric models increase the spatial resolution of census data by incorporating related ancillary data layers. These include land cover data, elevation and slope information, and coastline imagery. This is an improvement over regular census data, where population counts are reported spatially by census blocks, block groups, and tracts [22]; and temporally with a resolution of one-year to 10-year cycles [23]. For blocks, it assumes a uniform population distribution within them. Similarly, for block groups, it assumes uniform distributions at their polygonal centroids. Census data are therefore constrained spatially and temporally and do not capture the population dynamics in space and time. LandScan increases spatial and temporal resolution by using multiple information layers available at local scales. The LandScan USA dataset represents ambient population at 90 m resolution anywhere in the United States [23]. A higher 30-m-resolution LandScan USA dataset is of restricted access and can only be used by government agencies. Albeit one of the population datasets with highest resolution, LandScan involves a substantial level of analyst intervention to validate input data and modeling parameters, to improve model outputs. It may also have reduced accuracy along transition areas between urban and rural areas [24].

In previous literature, LandScan data have been used for mapping global impacts from climate change, building and evaluating population density models, mapping spread of dangerous diseases, and much more [25–27]. However, to our knowledge, LandScan data have never been used for the purpose of determining the lowest risk ground impact point for a UAV experiencing a hazardous flight anomaly. In the perspective of prior related art, as described earlier in this paper, there is still a need for a comprehensive ground impact mitigation system. The contribution of this paper, which builds on our previous work [28], is the integration of a novel ground impact and decision-making model with a high-resolution population dataset to provide high-accuracy collective risk profiles for safer UAV response. This work provides feasible ground impact footprint formulations and fault mitigation techniques for one propulsion mode and three types of combined actuator and propulsion modes, in addition to their corresponding simulation results and analysis. We show that with the ground impact and hazard mitigation (GIHM) module developed in this work, fatalities per flight hour were decreased on average by 41.97% and by up to 97% near populated areas.

The following sections of this paper are structured as follows: Sec. II describes the architecture and requirements of GIHM; Sec. III develops the feasible ground impact footprint models; Sec. IV details the fault modes and safest response; and Secs. V and VI present a case study, discussion, and conclusions.

II. Context-Level Architecture and Requirements

One of the biggest challenges in developing safer UAV flight control software is the ambiguous definition of system requirements and the lack of systems engineering diagramming. Before beginning development of GIHM, we provide systems architectural artifacts and requirements. Specific requirements and architectures are needed when tackling autonomous decision making [29].

A. Context-Level Architecture

We begin by presenting the block definition diagram (BDD) and internal block definition diagram (IBD) for GIHM. Figure 1 shows the system domain BDD for the ground impact and hazard mitigation module. The diagram provides a definition of the system and its environment in terms of the principal elements. GIHM comprises three elements: fault mode detection, UAV ground impact, and safest response. The GIHM system interacts with its external systems, which consist of the UAV flight software, flight states, and the LandScan population dataset. The user initiates the flight by entering the mission plan in the form of waypoints and uploads the area of operation data from LandScan.

Figure 2 details the context level IBD for GIHM. This IBD identifies how the system interacts with its user and external systems, its system boundaries, and state flows (data exchanged between blocks) between the system of interest, the user, and external systems. The state flows for GIHM include the mission plan in the form of waypoints, UAV states sent to GIHM (e.g., GPS coordinates, airspeed, roll, pitch, and yaw), and updated UAV states sent to the user. While GIHM was used fully autonomously in simulation (no input from the user after flight initiation), the level of autonomy can be adjusted to allow the user to be involved in the decision to use the new priority waypoints generated by GIHM.

The system context BDD also shows that the UAV flight software sends data real time to GIHM, and GIHM determines if there is a critical flight anomaly with the goal of minimizing its ground impact. Before flight, the user selects from LandScan data the area of operation for the UAV and uploads those data for use in case of a flight anomaly. From these data, GIHM can send new waypoints to the

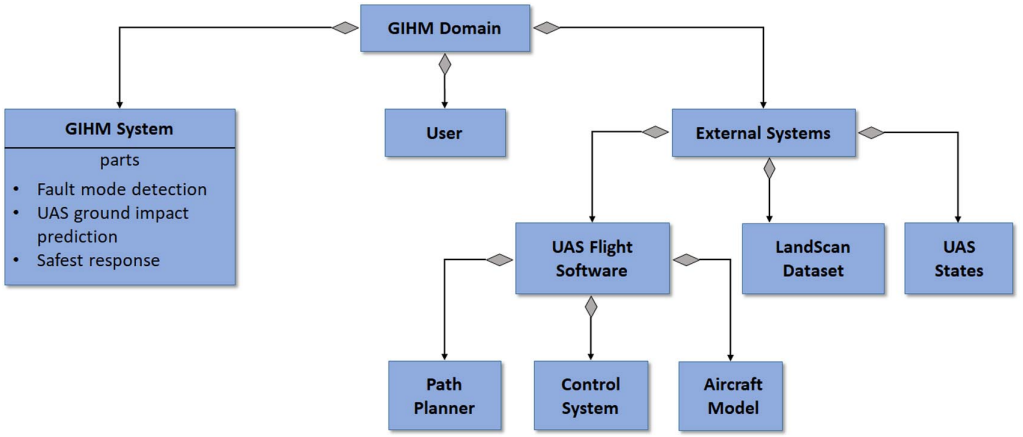

Fig. 1 GIHM system domain definition BDD. This establishes the domain of the system, which contains the GIHM system, user, and external systems.

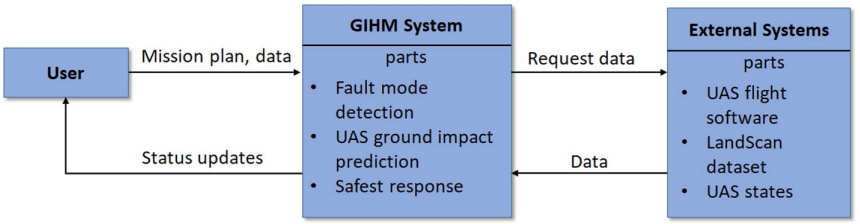

Fig. 2 GIHM context level IBD. This shows how the system interacts with its user and external systems.

UAV flight software, where the software executes the new mission plan.

B. System Requirements

Having presented two of the key architectural artifacts, we now develop the requirements for GIHM. To do this, we must identify a metric to quantify the safety of a UAV. Collective risk is the most commonly used metric in UAV ground models because it describes the aggregate risk to a population [3]. This metric has units of casualties per flight hour and shall be reduced by using UAV flight control software with GIHM. Results are generally dependent on the specific population scenario. GIHM is designed to reduce the number of casualties from UAV operations, and thus its collective risk. To accomplish this, the following system requirements need to be established where GIHM shall 1) determine the UAV's flight states (e.g., GPS coordinates, airspeed, roll, pitch, yaw); 2) predict the feasible ground impact footprint (FGIF); 3) use the FGIF to extract local population count map from LandScan data; 4) process the LandScan local population count map to extract lowest hazard zones as a candidate for landing; 5) select the safest hazard response; and 6) generate a revised UAV flight plan to implement safest response.

When an anomaly is detected by the decision-making module, GIHM must analyze the anomaly and determine which fault mode the aircraft is in. A fault is defined as an unallowed deviation of at least one characteristic property of the system from its standard operating condition [30]. Data-driven fault detection methods include checking limits on signal values and data trends. One approach is to detect an anomaly by comparing current measured UAV states to expected ranges of vehicle states (e.g., airspeed, thrust, Euler angles, angular rates, system components, and actuator deflections) [30]. If any of the values are deemed to be out of their expected operating range, a corresponding fault mode is diagnosed. One of the indicators of an inoperative engine is a sustained decrease in thrust, causing the aircraft to deviate from its course, and may pose a safety threat to nearby population in urban and suburban areas. For this work, the following four fault modes are considered:

1) The first fault mode is engine failure, which is UAV engine malfunction, resulting in no thrust.

2) The second fault mode includes engine and rudder failure, which is UAV engine and rudder control surface failure. The rudder control surface is stuck at the deflection it had during the time of the fault.

3) The third fault mode includes engine and elevator failure, which is the UAV engine and elevator control surface failure. The elevator control surface is stuck close to trim deflection. The trim value was chosen, as opposed to some value above trim, because it is of less severity and there is still some level of controllability over the new dynamics caused by the fault [31]. Additionally, this work does not consider any fault reconfiguration or reallocation methods.

4) The fourth fault mode includes engine and ailerons failure, which is the UAV engine and aileron control surfaces failure. The aileron's control surface is stuck close to trim deflection, for similar reasons as those stated for the third fault mode.

After detection and diagnosis of a flight anomaly, GIHM then projects the feasible ground impact footprint using gliding flight equations and current UAV states. GIHM extracts the local population data from LandScan, which is preloaded by the user before flight is initiated. Population data are then processed, with the lowest hazard zones identified. Based on these, GIHM selects the safest hazard response. The safest response consists of a new set of waypoints that the UAV follows to crash, assuming a safe landing zone is unfeasible. This response is a function of the collective risk in the identified reachable zone and whether the starting or ending waypoints are within the FGIF. Finally, GIHM sends the new mission waypoints to the UAV flight control software for implementation. Because this work does not focus on landing site determination, the waypoint that GIHM provides can be considered a crash point. This work also does not consider effects of winds or turbulence; these are part of future work.

C. GIHM Integration with UAV Flight Software

GIHM interfaces with a 6-DOF flight simulation software of a small fixed-wing UAV developed in MATLAB/Simulink. Figure 3 shows how GIHM interfaces with the flight simulation software at a top level. The standard flight simulation architecture contains a path planning block, a control system block, and an aircraft block.

The path planning block takes the initial three-dimensional mission waypoints and calculates desired values so that the UAV can reach them. These values go into the autopilot, which uses altitude

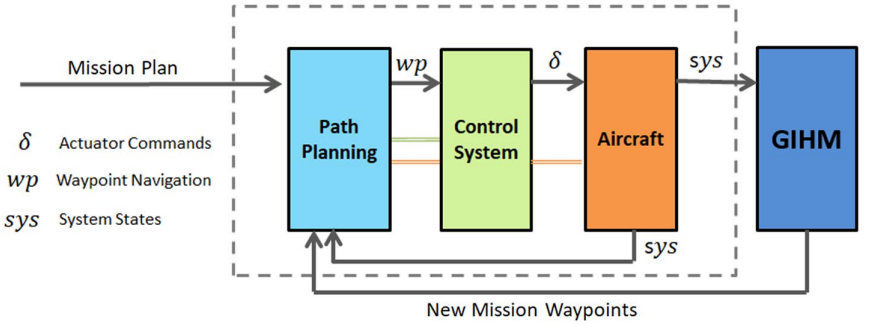

Fig. 3 Top level GIHM integration with UAV flight software. Components inside dashed box contain standard UAV flight software architecture. GIHM takes UAV system states as input and outputs new mission waypoints if a flight anomaly is detected.

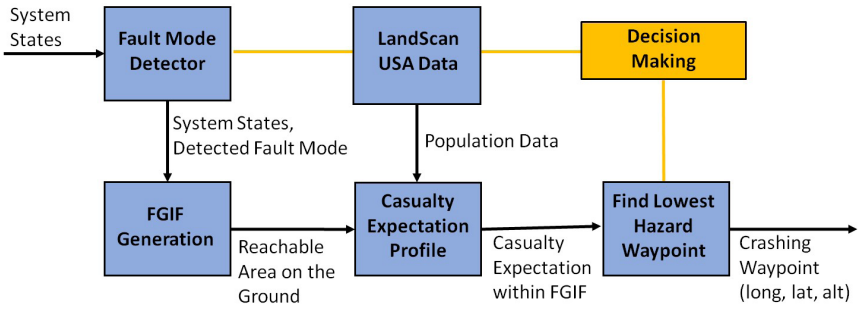

Fig. 4 Low level block flow diagram for GIHM. Inside GIHM, there is a fault mode detector block, a FGIF generation block, a LandScan USA Data block, a casualty expectation profile block, and a find lowest hazard waypoint block.

and lateral-directional control for trajectory tracking via proportional-integral-derivative (PID) controllers. It then uses the desired navigation requirements to output actuator commands to the UAV. Finally, the aircraft block, which houses the UAV aircraft model, takes in actuator commands to update the new system states. The aircraft model uses aerodynamic forces and moments, and it incorporates environmental factors related to altitude for air density and dynamic pressure calculations.

Figure 4 shows a low-level flow diagram detailing how GIHM processes the system states and outputs crashing waypoints if a fault mode is detected. The UAV states are sent to GIHM, where GIHM determines whether the UAV is experiencing a fault mode. It then generates a casualty expectation profile using LandScan USA data based on the feasible footprint, and chooses the lowest hazard waypoint.

In this work, a flight anomaly is detected when the UAV aircraft states are outside of a predetermined nominal range. If a fault mode is detected, GIHM sends back new mission GPS coordinates to the UAV flight control software. These new coordinates replace old mission waypoints.

III. Feasible Ground Impact Footprint

With the system architecture and requirements established, we now move into model development for GIHM. To fulfill its requirements, GIHM must accurately predict everywhere on the ground the UAV can reach. This is also known as the aircraft's feasible ground impact footprint. We used gliding equations for the FGIF calculations due to the choice of simulating a prevailing engine fault. Figure 5 depicts the axis representation used in development of the FGIF models. Variables d_x and d_y represent displacements in the longitudinal and latitudinal directions, respectively, and d_z represents displacement in altitude. The gliding flight equations were iterated over an aircraft's 360 deg of maneuverability to obtain a full reachable envelope. In Fig. 5, the red dashed line represents a trajectory to a crashing point without the inclusion of casualty expectation profiles, whereas the gray dashed line represents the lowest hazard crash waypoint selected by GIHM within the reachable footprint.

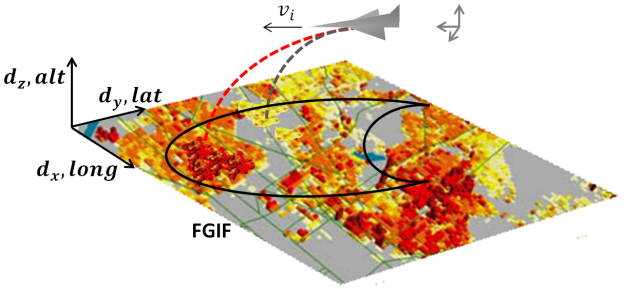

Fig. 5 Depiction of FGIF and coordinate system, where d_x, d_y, and d_z represent displacement in longitude, latitude, and altitude directions, respectively. UAV's reachable footprint is represented by semicircle contour labeled FGIF.

A. Gliding Flight

Calculation of the FGIF requires the vehicle's initial latitude, longitude, altitude, airspeed, roll angle, pitch angle, and yaw angle. These values are obtained from the UAV flight control software. The equations of motion in the aircraft's longitudinal, lateral, and vertical axis are, respectively [32],

$$m\frac{dv}{dt} = -mg\sin(\theta) - D + T\cos(\theta) \tag{1}$$

$$mg\cos(\theta)\sin(\phi) = mv\dot{\psi}\cos(\theta)\cos(\phi) \tag{2}$$

and

$$mg\cos(\theta)\cos(\phi) - L - T\cos(\theta) = -mv\dot{\psi}\cos(\theta)\sin(\phi) \tag{3}$$

where ϕ, θ, and ψ are the roll, pitch, and yaw angle, respectively. Also, $\dot{\psi}$ is the turn rate of the aircraft, m is the aircraft's mass, g is acceleration of gravity, D is drag, L is lift, and T is thrust. From here, we make the following assumption: for an engine out case, we set $T = 0$, resulting in gliding flight. If a small glide angle approximation

is used (which is the case for most aircraft), the gliding flight equations are simplified to

$$0 = -mg\sin(\theta) - D \tag{4}$$

$$\tan(\phi) = \frac{v\dot{\psi}}{g} \tag{5}$$

$$mg\cos(\phi) - L = -mv\dot{\psi}\sin(\phi) \tag{6}$$

Equations (4–6) are the three primary equations of motion for gliding flight in the aircraft's longitudinal, lateral, and vertical axes.

B. Footprint Calculation

In this work, the footprint consists of all the possible locations on the ground that the aircraft can glide to. This gliding range calculation consists of projecting how far the aircraft can travel during turning and level flight [16]. It is important to note that these calculations require dynamic access to vehicle states, e.g. Euler angles, velocities, as well as aerodynamic parameters from the aircraft model. Figure 6 shows an illustration of the construction of the footprint, with reference direction due north, or the y direction in this figure.

The total footprint is calculated by adding total distances traveled during the turning $(d_{x,t}, d_{y,t})$ and straight level phases $(d_{x,s}, d_{y,s})$:

$$d_x = d_{x,t} + d_{x,s} \tag{7}$$

$$d_y = d_{y,t} + d_{y,s} \tag{8}$$

This results in the following equations for distance traveled in the xy directions during gliding flight [16]:

$$d_x = R\sin(d\psi) + D_{\text{glide}}\sin(d\psi) \tag{9}$$

$$d_y = R\cos(d\psi) + D_{\text{glide}}\cos(d\psi) \tag{10}$$

where d_x and d_y are the coordinates at the end of the glide, relative to the initial position and heading of the aircraft. The FGIF therefore comprises all of the possible d_x and d_y combinations that the aircraft can reach.

The total ground distance traveled in the straight level flight, D_{glide} is calculated using the following equation [16]:

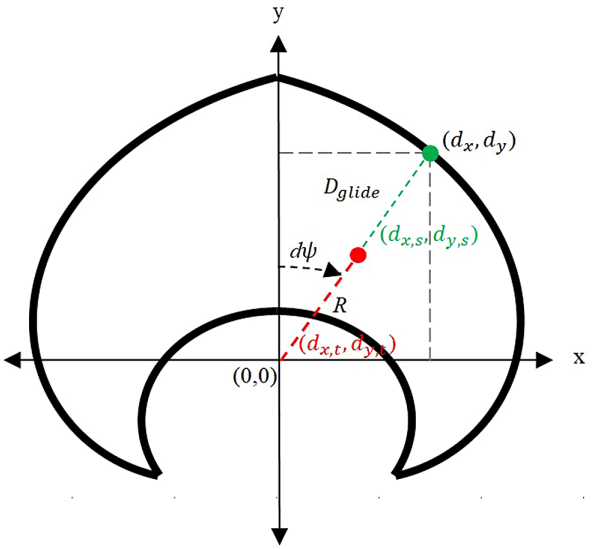

Fig. 6 Glide range geometry representation: The reachable footprint (FGIF) includes points generated in the turning phase and straight level phase flight of the UAV, centered at (0,0).

$$D_{\text{glide}} = (h_i - \Delta h_{\text{turn}})\frac{v}{v_s} \tag{11}$$

where h_i is the aircraft's initial height before entering gliding flight, where it is required that $|\Delta h_{\text{turn}}| < |h_i|$. To calculate the aircraft's height loss during the turning phase, we use

$$\Delta h_{\text{turn}} = L_{\text{arc}}\frac{v_s}{v}\sec(\phi) \tag{12}$$

where L_{arc} is the arclength of the circle made by the turn and is calculated as follows:

$$L_{\text{arc}} = Rd\psi \tag{13}$$

$$R = \frac{v^2}{g\tan(\phi)} \tag{14}$$

R is the radius of the circle, and $d\psi$ is the total change in heading. Also, $d\psi$ is bounded between $\pm\pi$ to account for an aircraft's ability to turn in the positive and negative directions. It is important to note that the optimal bank angle to maximize footprint extent is a function of heading change [33]. In this work, we only use a single bank angle in our formulation, but it can be extended using the analysis found in Ref. [33]. The choice of bank angle in our work is a result of requiring optimum turn conditions because a larger bank angle in the gliding turn phase requires a higher rate of descent to maintain steady conditions. The greater the bank angle in a steady-state gliding turn, the greater the rate of descent necessary to maintain steady-state conditions while in the turn [34]. Following derivations found in Refs. [16,34,35], we minimize altitude loss for a given change in heading angle, which amounts to minimizing the sink rate to airspeed ratio.

An aircraft's rate of sink v_s is the amount of height loss per unit time the aircraft is flying during gliding flight. Also, v_s is related to the aircraft's velocity, drag, and weight through the following equation [32]:

$$\frac{v_s}{v} = \frac{D}{W} \tag{15}$$

To calculate drag, we use equations from Ref. [36]:

$$D = 0.5C_D\rho_0 v^2 S \tag{16}$$

$$C_D = C_{D_0} + \frac{kC_L^2}{\pi A_r} \tag{17}$$

where ρ_0 is the density of air at sea level, S is the wing area, C_{D_0} is the aircraft's profile drag, and k is the induced drag factor, determined by the aircraft wing dimensions, configuration, Reynolds number, and Mach Number. A_r is the aircraft's wing aspect ratio, and C_L is the coefficient of lift.

The following equation was used to calculate C_L [37]:

$$C_L = C_{L_0} + C_{L_\alpha}\alpha \tag{18}$$

where C_{L_0} is the aircraft's coefficient of lift at a zero angle of attack, C_{L_α} is the angle-of-attack stability derivative, and α is the aircraft's angle of attack. This equation is valid for a small angle of attack. Since the aircraft is not approaching stall conditions, the aircraft's angle of attack will be within the linear region of the angle of attack vs the coefficient of lift relationship.

It is important to note that, for this work, it is assumed that there is no wind, which would otherwise have an effect on the gliding performance of a UAV [35]. In addition, the reference direction is adjusted to due east for integration with the flight software (Fig. 3). To this effect, an angle factor of $pi/2$ was added to Eqs. (9) and (10):

$$d\psi_{\text{east}} = pi/2 - d\psi \tag{19}$$

IV. Fault Modes and Safest Response

Now that models are established for gliding flight, we next investigate the effects the four fault modes have on gliding performance.

A. Fault Modes

Faults are defined as unpermitted deviations of at least one characteristic property or parameter of the aircraft system from the acceptable or standard condition [30]. The impact of a fault can be small, but it could also lead to overall system failure. After failure detection, a safe, autonomous system needs to be able to classify the fault into an appropriate category in order to mitigate its effects. Faults are classified according to where they occur in the system (i.e., sensors, actuators, and other components). Faults can also be classified as abrupt, incipient, or intermittent with respect to their time characteristics.

In this work, we consider an abrupt power system fault and combined abrupt power system/actuator faults. The actuator fault implemented in simulation consists of ailerons, rudder, and elevator surfaces stuck after a servo failure that either remains at the deflections they had at the time of the fault or remains close to trim value [6]. It was assumed in this work that the UAV is still controllable when experiencing these faults.

1. *Fault Mode 1: Engine Failure*

In this fault mode, it is assumed that the UAV cannot accelerate but can change its roll, pitch, and yaw angles. Because of this, the d_x and d_y in Eqs. (7) and (8) derived earlier are used in their entirety to calculate the FGIF.

2. *Fault Mode 2: Engine and Rudder Failure*

In this fault mode, it is assumed that the UAV cannot accelerate but can change its heading using the functioning ailerons. Even though the rudder is stuck at a specific deflection, the UAV may use its ailerons to adjust its heading. It was also assumed the aircraft's sideslip is minimal enough that it could still maneuver to various headings. The validity of this assumption is explored in Sec. V, where UAV trajectory and aircraft state plots are provided for the engine and rudder failure fault mode. Because of these assumptions, d_x and d_y equations derived earlier in this paper are used in their entirety to calculate the FGIF.

3. *Fault Mode 3: Engine and Elevator Failure*

In this fault mode, it is assumed that the UAV cannot accelerate or change its angle of attack but can change its heading. The UAV's elevator is stuck at its trim value, resulting in the aircraft not having the ability to change its angle of attack. This would result in the inability of the UAV to minimize its sink rate by changing its angle of attack. Because of this, d_x and d_y equations derived earlier in this paper are used in their entirety to calculate the FGIF, with the limitation of not being able to change its angle of attack to reach everywhere inside the maximum FGIF boundary.

4. *Fault Mode 4: Engine and Ailerons Failure*

In this fault mode, it is assumed that the UAV cannot accelerate or change its heading but can pitch. Based on our control setup, when the ailerons are stuck at trim value, the UAV is unable to change its heading because heading is only controlled by the ailerons and control reconfiguration is not used in this work. If the aircraft does not have heading control, it cannot execute a turning phase. Because the UAV cannot change heading, $d\psi = 0$, which results in only straight level flight. From this, the following modified gliding flight equations must be used to reflect that only straight level gliding flight can be achieved:

$$d_x = D_{\text{glide}} \sin\left(\frac{\pi}{2} - \psi\right) \tag{20}$$

$$d_y = D_{\text{glide}} \cos\left(\frac{\pi}{2} - \psi\right) \tag{21}$$

$$D_{\text{glide}} = h_i \frac{v}{v_s} \tag{22}$$

The D_{glide} term was modified to exclude the Δh_{turn} term because the aircraft is unable to turn. Notice that in the equations for d_x and d_y, the $d_{x,t}$ and $d_{y,t}$ terms were removed because the aircraft is not turning while experiencing this fault mode. This results in a straight line reachable footprint. While the trajectory of an aircraft with stuck ailerons may not always be a straight line path, it is assumed in this work that ailerons are stuck close to trim value, which results in straight line trajectory.

Figure 7 shows the effect of altitude on the FGIF of an aircraft traveling due north, experiencing fault mode 1. The aircraft's initial position when experiencing the fault mode is at the origin of the plots. Figure 7a shows the FGIF of an aircraft with a roll angle of 35 deg, at an altitude of 15 m. Figure 7b shows the FGIF projected at different heights. As the initial height of the aircraft increases, so does the FGIF, which is represented by the shaded area between the inner and the outer contours, as shown in Fig. 7a. This is because the aircraft is able to glide for a longer time, resulting in a larger footprint.

Figure 8 shows the FGIF of an aircraft traveling due north, experiencing fault mode 1 at different roll angles and different velocities. At smaller roll angles, the aircraft cannot execute turns to larger heading angles fast enough. As a result, the aircraft cannot reach those larger angles before landing. This is seen in Fig. 8a, where the aircraft experiences the fault mode while at small roll angles. Because of the small roll angle, the FGIF is only part of a circle. As the roll angle increases, the aircraft can more quickly maneuver to larger yaw angles, as shown in Fig. 7. The roll angle of the aircraft is for the turning phase of gliding flight only. Figure 8b shows the effect of velocity on the FGIF. When the aircraft slows down, it has access to a larger FGIF, whereas when it speeds up the reachable footprint decreases.

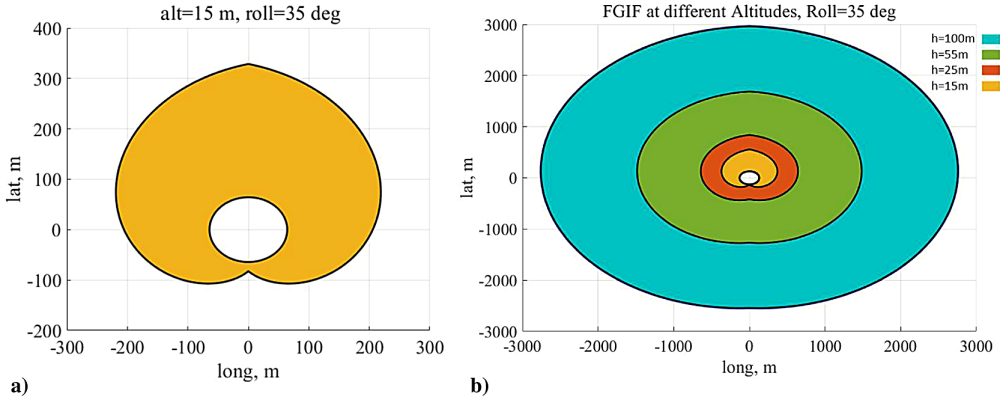

Fig. 7 Effect of aircraft height on FGIF for fault mode 1: a) alt = 15 m, roll = 35 deg, and shaded area is FGIF; and b) FGIF at different altitudes, with roll = 35 deg.

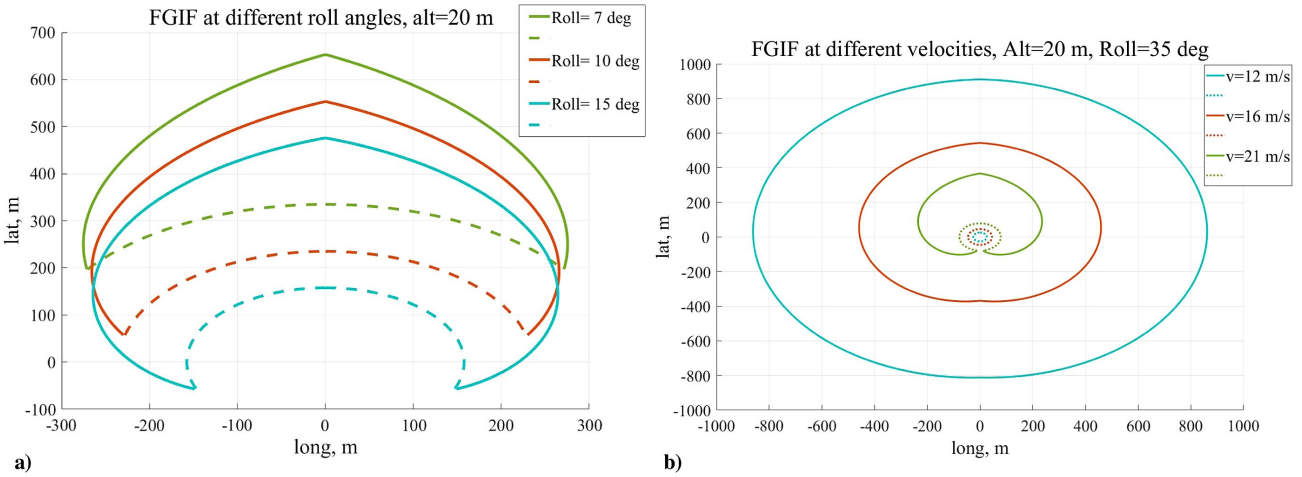

Fig. 8 Effect of aircraft roll angle and velocity on FGIF for fault mode 1: a) FGIF at different roll angles, with alt = 20 m; and b) FGIF at different velocities, with alt = 20 m and roll = 35 deg.

The FGIF of an aircraft experiencing the engine and rudder failure fault mode would have very similar characteristics as the engine failure fault mode. When the rudder is stuck, the ailerons are able to change the heading of the aircraft and allow for relatively straight line flight. However, there will be sideslip as a result of the rudder control being compromised. For this work, it is assumed that the sideslip is minimal enough to where the aircraft can still maneuver to the calculated crash zone. The FGIF of an aircraft experiencing the engine and elevator failure fault mode would have a similar FGIF as the engine out case, with the exception that the UAV cannot change its angle of attack to reach anywhere inside the maximum FGIF boundary. Therefore, the FGIF would be a contour. Finally, the FGIF of an aircraft experiencing the engine and ailerons failure fault mode would be a straight line. This is because with the ailerons stuck at trim value, the aircraft is unable to change its heading. However, the aircraft is able to change its angle of attack, resulting in a straight line FGIF, as opposed to a two-dimensional region.

B. Safest Response

With a model developed for the FGIF, we next develop a procedure for choosing the safest response within the reachable footprint. A searching algorithm takes the range of geodetic coordinates generated from the FGIF, and it extracts all of the population values from the LandScan-USA-based data within the range of geodetic coordinates. It then extracts the local minimum population value for which the UAV would pose the least collective risk. The data structure of LandScan is a matrix whose rows and columns represent latitudinal and longitudinal coordinates. The value of each matrix cell is the population for that range of geodetic coordinates. The LandScan USA dataset at 30 m resolution is restricted for use by government agencies only; however, the 90 m resolution dataset is freely available for universities. In this work, we use a simulated dataset at a 30 m resolution.

To determine safest response, we calculate the point of lowest collective risk within the FGIF. Collective risk, also known as casualty expectation CE, describes the aggregate risk that a UAV poses to a population of people. It is measured by the expected number of casualties per flight hour [3]. Collective risk is calculated using the following equations [10]:

$$CE = PF \cdot PD \cdot AL \cdot PK \cdot S \tag{23}$$

$$AL = (L + DG + DS + 2B) \cdot (W + 2B) \tag{24}$$

Definitions and the domain of variables for Eqs. (23) and (24) can be found in Table 1. Probability of failure PF is the expected number of mishaps per flight hour; population density PD is the population count per square meter; probability of a fatality PK is the probability of a piece of the UAV striking a pedestrian and leading to a fatality; and shelter factor S is an estimate of how exposed a population is to falling vehicles or debris, with factors of zero and one representing completely sheltered and completely exposed, respectively. The lethal area AL is the area where a fatality may occur if a vehicle or debris falls over it. The length L and width W refer to the wingspan and length of the aircraft, respectively; buffer B is a safety factor; glide distance DG is the distance traveled beginning when the UAV is at an altitude of 6 ft and ending when it reaches the ground; and distance to stop DS is the total distance from when the UAV reaches the ground to when it comes to a complete stop. Because it is assumed that the UAV will crash and not land, $DS = 0$.

The lethal area, length, width, glide distance, and distance to stop are all specific to the aircraft and aircraft dynamics. The upper range of population density is determined by the highest population density in the United States, located in Guttenberg, New York City. The resulting casualty expectation values can be as low as zero fatalities per flight hour and as high as 6.43 fatalities per flight hour. For large airliners, the average casualty expectation is 0.01 fatalities per 100,000 flight hours, and that of small general aviation aircraft is 0.1 fatalities per 100,000 flight hours [2]. However, the casualty expectation will be much higher than these values for UAVs because casualty expectation is proportional to probability of failure, and manned aircraft have very small probabilities of failure (0.000064%) compared to unmanned aircraft (2.17%) [38,39]. This leads to a collective risk for small UAVs that is expected to be nearly 100,000 times larger than that of a manned aircraft.

For the purposes of this paper, probability of failure was assumed to be 0.0217, consistent with the maximum probability of failure for a small UAV defined in Ref. [39]. The population density was found by dividing the population count from the LandScan data by its respective area. The probability of fatality was calculated using methods

Table 1 Definitions of variables in casualty expectation equations

Variable	Definition	Domain
CE	Casualty expectation	[0, 6.43] fat/flt hr
P	Probability of failure	(0, 1]
PD	Population density per square meter	[0, 0.022] pop/m^2
AL	Lethal area	77.75 m^{2a}
PK	Probability of fatality	[0, 1]
S	Shelter factor	[0, 1]
L	Length	1.83 m^a
W	Width	1.41 m^a
B	Buffer	1 ft
DG	Glide distance at 6 ft altitude	8.02 m^a
DS	Distance to stop	0 m

[a]These do not have a range of values because they are highly specific to the aircraft's dynamics. Representative values were given for the UAV simulated in this work.
Fat/flt hr = fatalities per flight hour.

explained by the Range Safety Group, which was a function of the mass and speed of the aircraft [10]. A conservative shelter factor of one was used, representing a fully exposed population. Glide distance was calculated using the following equations [40]:

$$DG = \tan\left(\frac{H_p}{\gamma}\right) \tag{25}$$

$$\gamma = \tan^{-1}\left(\frac{h}{d}\right) \tag{26}$$

where γ is glide angle, H_p is the height of an average person, and d is the ground distance traveled from when the aircraft is at height h until when it hits the ground. For calculation of CE, $h = H_p$. Note that this glide distance is different than the glide distance derived in Sec. III because this is the glide distance starting when the vehicle is at height H_p and not its mission plan height. By knowing the collective risk profile within the FGIF, the UAV is now able to find the point of local minimum risk and decide if the safest response is to fly to that minimum risk waypoint.

Also note that while the population data are always available, it may not always be required in determining the safest response. If the mission endpoint is within the FGIF of the aircraft, then the UAV should naturally land at that waypoint as its the safest response. Similarly, if the mission endpoint is not within the FGIF but the mission start is, then the aircraft should fly back to where it started.

V. Case Study and Discussion

A. Problem Setup

With the models and algorithm logic developed, we now present a case study to show the utility of GIHM integrated with standard UAV flight control software. In this case study, we model a small fixed-wing UAV. The aerodynamic characteristics used for the small UAV are given in Table 2.

The UAV's nominal mission plan contains five waypoints and a home waypoint. The waypoints approach the University of Maryland, and a given fault mode is induced into the simulation 35, 45, 65, 80, 100, and 115 s into the simulation. These times were chosen to obtain a wide range of flight scenarios with the UAV at different points during its mission.

Model LandScan data were created in MATLAB that replicated the structure of LandScan USA data but with a resolution of 30 m. The finer resolution was required to show the utility of GIHM for small UAVs because of the size of the FGIF during simulations. Fixed blocks of higher population were created to mimic higher population expected in clusters of buildings at the University of Maryland. The dataset was preloaded into the UAV simulation and was parsed in real time when a fault mode was detected.

B. Results and Discussion

1. Casualty Expectation Reduction

This section presents numerical results for the testing of GIHM. Table 3 summarizes the results of simulations for all four fault modes at six fault mode times. By examining the average casualty expectation, we can conclude that the average casualty expectation is 23.014 fatalities per 100,000 flight hours lower with the GIHM module than without the module, for the simulation set used. This equates to a 97.5% decrease in fatalities per flight hour for these chosen scenarios. The percent decrease in CE with GIHM will vary depending on the magnitude of population density gradients in the area the UAV is flying. Note that the units in Table 3 have units of fatalities per 100,000 flight hours, whereas CE has units of fatalities per flight hour in Table 1.

According to the Federal Aviation Administration, a large airliner shall have a casualty expectation of one fatality per 1,000,000 flight hours, which is still far below the average casualty expectation value for the UAV with GIHM. This is because the probability of failure for this simulation is 2.17%, which is nearly 300,000 times higher than the probability of failure for a large airliner (0.000064%).

Table 2 Characteristics of the general aviation UAV used in simulation

Variable	Definition	Value
v	Aircraft velocity	20 m/s
$\alpha_{\max}$	Max angle of attack	6.25
m	Maximum takeoff weight	1.2 kg
L_w	Wingspan	1.4 m
T_w	Wing taper	1.95
AR	Wing aspect ratio	6.4
w_c	Wing aerodynamic chord	0.22 m
airfoil	Wing airfoil	SD7037
C_{Li}, C_{Di}, C_{Mi}	Lift, drag, moment coefficient derivatives	From airfoil

Table 3 Simulation results comparing CE with and without the GIHM module for all four fault modes at six different fault times[a]

Fault mode	Fault time, s	CE with GIHM	CE without GIHM
1	35	0.000	2.315
2	35	0.000	2.315
3	35	1.329	12.42
4	35	0.057	5.736
1	45	0.026	115.200
2	45	0.026	115.200
3	45	0.233	14.820
4	45	4.010	63.950
1	65	0.026	15.180
2	65	0.026	15.180
3	65	0.310	8.625
4	65	0.500	0.500
1	80	0.026	13.770
2	80	0.026	13.770
3	80	0.017	8.633
4	80	1.062	5.515
1	100	0.026	33.400
2	100	0.026	33.400
3	100	3.413	5.151
4	100	1.096	16.570
1	115	0.041	19.190
2	115	0.041	19.190
3	115	1.103	2.683
4	115	0.055	0.469
Average	— —	0.584	23.598

[a]CE has units of fatalities per 100,000 flight hours.

2. UAV Mission Simulations Results with GIHM

With numerical results presented, we assume that the UAV can maneuver to and reach the low hazard waypoint provided by GIHM. This section provides the trajectory and aircraft states profiles for the simulated UAV. The trajectory and aircraft states profiles are presented for when the UAV does not experience any fault modes and when the UAV experiences the four fault modes. These results show the limitations and maneuverability of a UAV experiencing various fault modes. They will also provide evidence that the FGIFs and low hazard waypoint provided by GIHM accurately model where the UAV can glide to.

a. Nominal Flight Mode. Figures 9 and 10 show the flight simulation trajectory and altitude profile of the UAV under nominal operating conditions. The simulation starts with the UAV at the home location and ends after the UAV reaches the fifth (final) waypoint. The trajectory plots show the relative distance the UAV travels with respect to the home waypoint. On all of the trajectory plots, the heat map represents population count in that node, with darker nodes representing highly populated areas. The population heat map is pixilated because the data were generated using randomized values. The randomized values were generated based on average population values in the University of Maryland area.

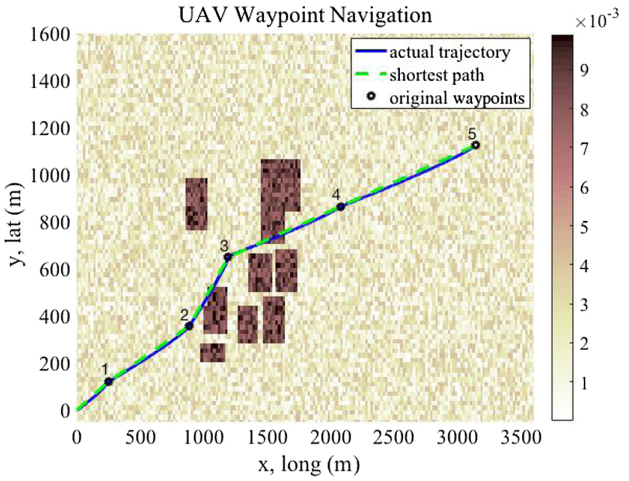

Fig. 9 UAV trajectory without fault modes: aircraft starts from home waypoint at origin and travels to the waypoints in numerical order.

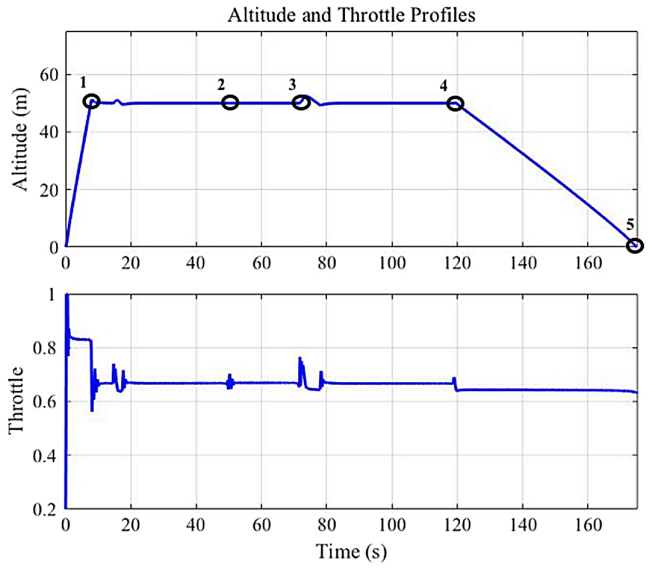

Fig. 10 UAV altitude and throttle profiles for when no fault mode detected. Five mission waypoints represented by numbered circles. UAV starts on ground, climbs to altitude of 50 m, and then descends back to ground when approaching waypoint 5.

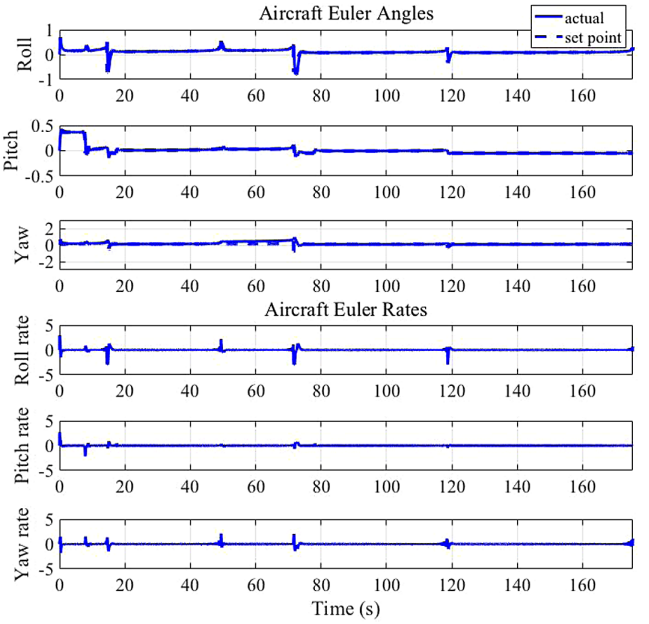

Fig. 11 UAV Euler angles and rates profiles for UAV trajectory without fault modes. Angles in radians. Dashed lines on Euler angle plots show controller commands, and solid lines show actual aircraft states.

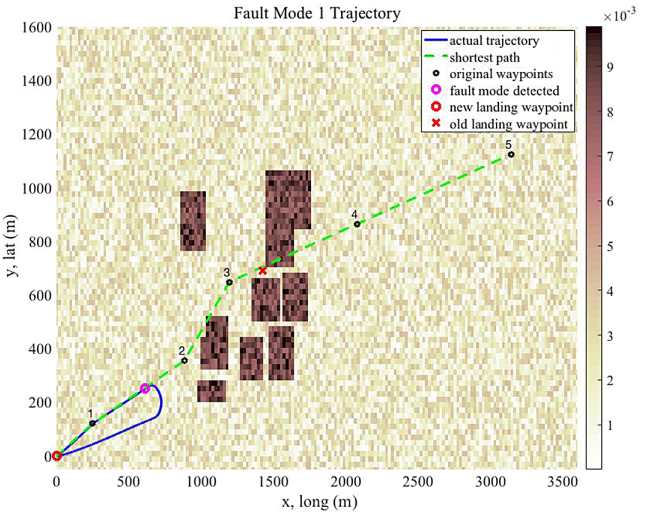

Fig. 12 UAV trajectory for when fault mode 1 detected at 35 s. Aircraft starts from home at origin and travels to waypoints in numerical order until fault mode detected. In this scenario, GIHM determined home location within reachable footprint and UAV could return to it.

It can be seen from the trajectory plot (Fig. 9) that the actual flight path of the UAV is very close to the shortest path, indicating an effective path tracking scheme. Figure 11 shows the Euler angle and Euler rate profiles for the nominal flight simulation, where no fault modes are being considered.

Now that the nominal mission plan and UAV states have been presented, we next examine how the mission plan would change when the UAV experiences different fault modes. Trajectory plots are provided for each fault mode, but the UAV states and specific control surface and altitude plots were only presented for fault mode 2 in the interest of space, and because it provides the most interesting results.

b. Fault Mode 1. Figure 12 shows the simulated flight trajectory of the UAV undergoing an engine failure (fault mode 1) 35 s after flight initiation. This trajectory plot shows the utility of the return to base function for GIHM. When the engine failure fault mode was detected, GIHM determined that the home waypoint was within the FGIF, and the UAV was able to return home. This resulted in a casualty expectation of zero fatalities per 100,000 flight hours, which is also reflected in Table 3. The new landing waypoint is the waypoint sent by GIHM upon detection of the fault, and the old landing waypoint is where the UAV would have landed without GIHM.

c. Fault Mode 2. Figures 13 and 14 show simulation results of the UAV experiencing an engine and rudder failure (fault mode 2) 50 s after it starts its mission plan. Figure 13 shows the flight trajectory, where a new waypoint is found by GIHM to prevent the aircraft from crashing into a populated area as a result of the fault mode. Figure 14 shows the altitude profile, where the aircraft descends to a new waypoint.

At 50 s, as the UAV approaches waypoint 2, the engine and rudder failure fault mode is detected, which produces a change in heading and change in mission plan. To find the "old landing waypoint" in Fig. 13, or where the UAV would have landed without GIHM, the simulation is run with the UAV continuing on in its initial mission plan, even when the fault is detected. The old landing waypoint is where the UAV is found when its altitude equals zero.

The new landing waypoint is in a less populated spot compared to the old landing point. A safety factor of 30 m was included to ensure the UAV does not land adjacent to the highly populated cluster of buildings. Figure 13 shows that sideslip is minimal when the rudder is

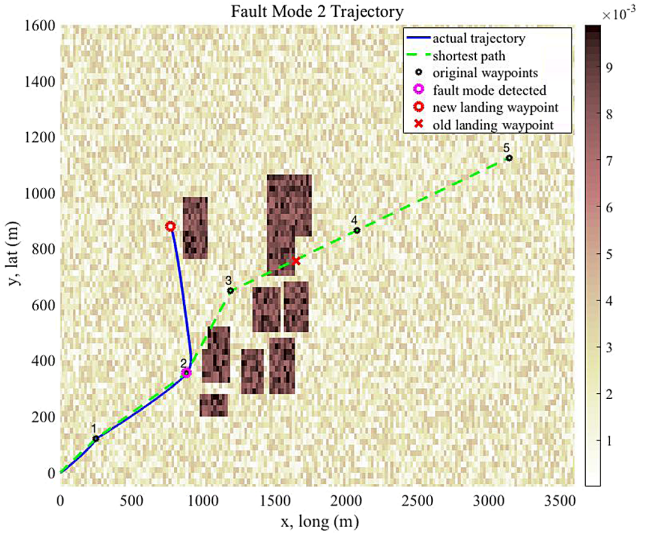

Fig. 13 UAV trajectory for fault mode 2: aircraft starts its mission at home location and travels through waypoints in sequence. Its original mission plan is interrupted when fault detected at 50 s. GIHM calculates a new landing waypoint for UAV.

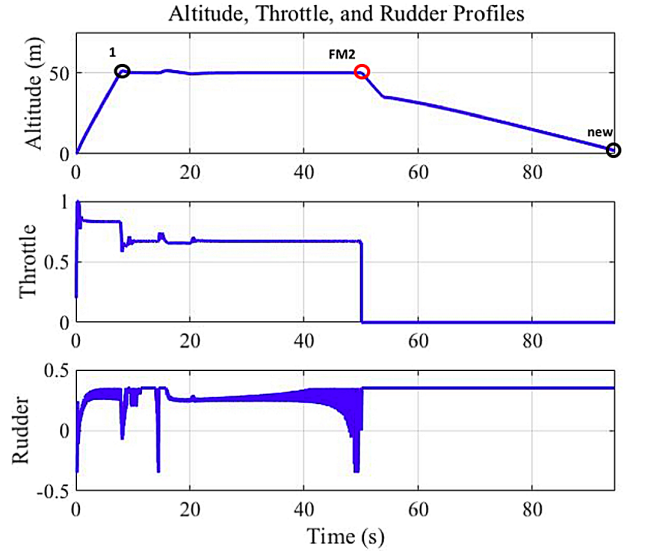

Fig. 14 UAV altitude, throttle, and rudder profiles for when fault mode 2 detected at 50 s. Mission waypoints represented by numbered circles, with one labeled "new" corresponding to new landing waypoint generated by GIHM. Red circle represents when fault mode detected.

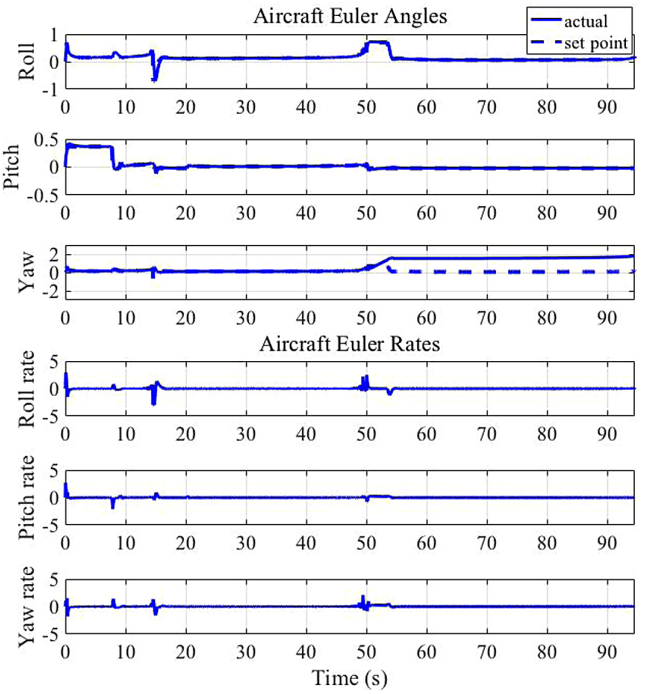

Fig. 15 UAV Euler angles and rate profiles for when fault mode 2 detected at 50 s. Angles in radians. Dashed lines on Euler angle plots show controller commands, and solid lines show actual aircraft states.

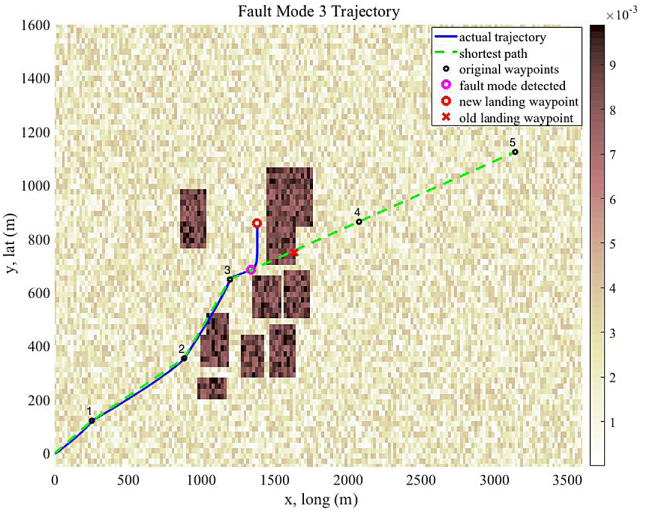

Fig. 16 UAV trajectory for hazard mitigation when UAV experiences fault mode 3. Aircraft starts from home location and follows mission waypoints in numerical sequence until fault mode detected at 80 s. New landing waypoint calculated by GIHM.

stuck and that the ailerons are sufficient in guiding the aircraft to the low hazard waypoint. Figure 14 shows the time histories of the throttle and rudder of the UAV when it undergoes fault mode 2 50 s into the flight. At 50 s, the throttle is at zero and the rudder is stuck at 0.3 rad, which is consistent with the conditions of the engine and rudder failure case. The trajectory and altitude plots for this fault mode case show that the UAV has found a minimum hazard impact point on the ground and that it flies to it, safely terminating its flight.

Figure 15 shows the Euler angles and Euler rates for the UAV experiencing fault mode 2 50 s after flight initiation. Note the change in Euler angles at the time of 50 s, which is a result of the aircraft changing heading to fly to the new priority waypoint generated by GIHM.

d. Fault Mode 3. Figure 16 shows the simulated flight trajectory of the UAV undergoing an engine and elevator failure (fault mode 3) 80 s after mission plan initiation. The trajectory plot shows the UAV maneuvering to the lowest hazard waypoint, as opposed to continuing on its mission plan. If it continued on in its mission, the casualties per flight hour would have been much higher because it would have landed in a much higher populated area.

e. Fault Mode 4. Figure 17 shows the simulated flight trajectory of the UAV experiencing a flight anomaly consisting of engine and ailerons failure (fault mode 4), which is detected 45 s after flight initiation. The trajectory plot shows that even when the ailerons are stuck at trim value, the aircraft is still able to fly in a straight line path and change its elevator deflection to reach the lowest hazard waypoint. If the UAV continued on its nominal mission plan, then it would have ended up flying over and crashing in a highly populated area.

Monte-Carlo-type simulations were conducted for fault mode 1, which provides less dependency on aircraft states because the aircraft is able to maneuver fully using all three remaining control surfaces. Two representative sets of scenarios were chosen; one where the UAV

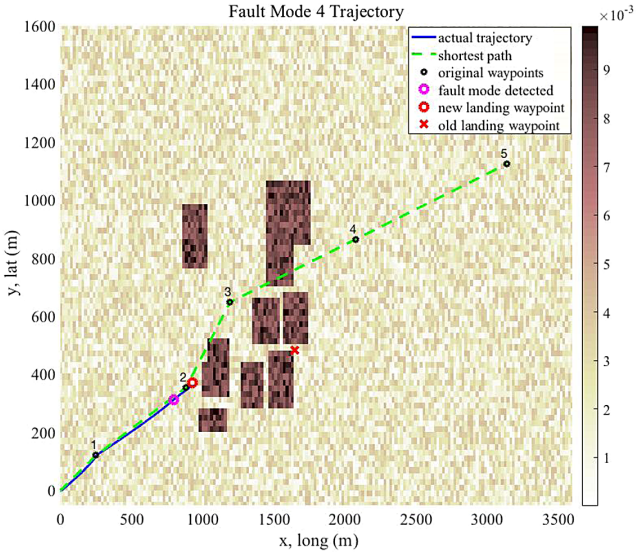

Fig. 17 UAV trajectory for hazard mitigation when UAV experiences fault mode 3. Aircraft starts from home location and follows mission waypoints in numerical sequence until fault mode 4 detected at 40 s. New landing waypoint calculated by GIHM.

experienced the fault over an area with low population, and one where the UAV experienced the fault in the vicinity of a highly populated area. A batch file was generated to run random combinations of fault times, and therefore of UAV locations at time of fault onset. Random locations of a large population of high population density were also studied. The UAV targeted path and waypoints remained the same for this set of runs. Fault times varied between $t = 50$ to 500 s with a total run time of 600 s.

Results show that the rate of success is lower around low population areas and higher in the vicinity of highly populated areas. The simulation results shown in Table 4 entail 300 simulations total. It shows that decrease in casualty expectation is higher when the UAV experiences a fault near highly populated areas. The casualty expectation with GIHM entails choosing a crash point with minimal hazard to population. The casualty expectation without GIHM refers to the casualty expectation associated to a crash point that does not consider any mitigating factors, and it corresponds to where the UAV would have landed as a result of experiencing a fault.

In all the fault modes studied, it was shown that after detection of a fault mode, GIHM successfully calculated a new waypoint with lowest ground impact based on casualty expectation estimates. The new waypoints generated by GIHM in all the fault cases successfully avoided the highly populated areas, whereas the UAV could have landed on highly populated zones had the UAV not made use of the GIHM module. It was observed that fault modes that allow for heading changes require more computation time because of the added amount of data points in the FGIF. The design of the GIHM module allows for real-time implementation of safe reactions to anomalies. On average, the computation time of the GIHM module is 0.03 s, as run by a 2015 1.6 GHz I5 processor. The overall computation time of all simulation components (aircraft, controller, path planner, and GIHM module) is 9.64 s as run by a 2017 quadcore i7 at 2.60 GHz.

Table 4 Simulation results comparing CE with and without the GIHM module for fault mode 1[a]

Fault time, s	CE with GIHM	CE without GIHM	Maximum decrease CE, %
Low population	23.36	28.05	16
High population proximity	24.86	97.18	69.92
High and low aggregate total	23.76	57.27	40
Average	23.99	60.83	41.97

[a]CE has units of fatalities per 100,000 flight hours.

Monte-Carlo-type simulations were run in a 2019 hexacore i7 processor at 4.6 GHz.

VI. Conclusions

This work entails the development of a hazard mitigation module that guards against ground impact in highly populated areas. The module combined a reachable ground footprint model with a precise synthetic population dataset with LandScan USA data properties. It was integrated with a flight simulation software that included a 6-DOF aircraft model, path planning, and autopilot control.

Effectiveness of GIHM is higher when the UAV experiences a fault near highly populated areas. A set of statistical results for a propulsion failure show that the rate of success for reduction of the casualty expectation is lower around low population areas and higher in areas near highly populated regions. This is because GIHM finds a crash point that minimizes the casualty expectation within its reachable ground area. The success rates are higher when there are low population areas that the UAV can resort to when experiencing a fault. These rates might be further reduced, depending on the degree to which the fault hinders maneuverability. The fault modes in this work served to demonstrate the hazard mitigation capabilities of the GIHM module, given the restrictions that specific fault modes can cause. Simulation results show that the UAV reduced the casualty expectation for different flight anomalies, which consisted of propulsion and actuator faults.

Existing ground footprint models for UAV decision making either do not take into account population density in the reachable footprint or the population density data accuracy needs to be improved. The addition of a precise population dataset is important for development of reachable ground footprint models because the UAV now possesses the ability to quantify its ground impact after determining where it can land. This is especially useful to UAVs with short flight range because these might require population data models with higher resolution. This work can be expanded using additional temporal information that the LandScan database provides, allowing for dynamic calculations of casualty expectation.

Future work includes examining how uncertainties in different UAVs and environment parameters may affect the performance of GIHM, developing fault modes for accelerated aircraft experiencing various control surface malfunctions, exploring fault detection methods, integrating a collision detection and avoidance module, addition of topology data for landing site considerations, and a more sophisticated decision-making engine that allows the UAV to execute various flight control instability mitigation maneuvers during flight anomalies before diagnosing a fault mode.

Acknowledgments

The authors would like to thank the Maryland Industrial Partnerships Program and Millennium Engineering and Integration Company for their support of this project. We would like to thank Mike Briggs, Kerry Wisnosky, Ken Baird, and Adam Pederson from Millennium Engineering and Integration Company for their support and assistance in this work; and Zijie Lin from the University of Maryland.

References

[1] Chen, H., Wang, X.-M., and Li, Y., "A Survey of Autonomous Control for UAV," *International Conference on Artificial Intelligence and Computational Intelligence, 2009. AICI'09.*, Vol. 2, Inst. of Electrical and Electronics Engineers, New York, 2009, pp. 267–271.

[2] Loh, R., Bian, Y., and Roe, T., "UAVs in Civil Airspace: Safety Requirements," *IEEE Aerospace and Electronic Systems Magazine*, Vol. 24, No. 1, 2009, pp. 5–17. https://doi.org/10.1109/MAES.2009.4772749

[3] Wu, P. P., and Clothier, R. A., "The Development of Ground Impact Models for the Analysis of the Risks Associated with Unmanned Aircraft Operations over Inhabited Areas," *Proceedings of the 11th Probabilistic Safety Assessment and Management Conference (PSAM11) and the Annual European Safety and Reliability Conference (ESREL 2012)*, Curran Associates Inc., Red Hook, NY, 2012, pp. 5222–5235.

[4] Elias, B., "Pilotless Drones: Background and Considerations for Congress Regarding Unmanned Aircraft Operations in the National Airspace System," Congressional Research Service TR R42718, Washington, D.C., 2012.
[5] Neogi, N., Bhamidipati, K., Uhlig, D., Ortiz, A., and Krauss, J., "Engineering Safety and Reliability into UAV Systems: Mitigating the Ground Impact Hazard," *AIAA Guidance, Navigation and Control Conference and Exhibit*, AIAA Paper 2007-6510, 2007.
[6] Belcastro, C. M., Klyde, D. H., Logan, M. J., Newman, R. L., and Foster, J. V., "Experimental Flight Testing for Assessing the Safety of Unmanned Aircraft System Safety-Critical Operations," *17th AIAA Aviation Technology, Integration, and Operations Conference*, AIAA Paper 2017-3274, 2017.
[7] Israel, K., and Nesbit, R., "Defense Science Board Study on Unmanned Aerial Vehicles and Uninhabited Combat Aerial Vehicles," Defense Science Board TR ADA423585, Washington, D.C., 2004.
[8] Venkataraman, R., Lukátsi, M., Vanek, B., and Seiler, P., "Reliability Assessment of Actuator Architectures for Unmanned Aircraft," *IFAC-PapersOnLine*, Vol. 48, No. 21, 2015, pp. 398–403. https://doi.org/10.1016/j.ifacol.2015.09.559
[9] Lum, C., and Waggoner, B., "A Risk Based Paradigm and Model for Unmanned Aerial Systems in the National Airspace," *Infotech@Aerospace 2011*, AIAA Paper 2011-1424, 2011.
[10] "Range Safety Criteria for Unmanned Air Vehicles," Range Commander's Council TR 323-99, White Sands Missile Range, NM, 1999.
[11] Burke, D. A., Hall, C. E., Jr., and Cook, S. P., "System-Level Airworthiness Tool," *Journal of Aircraft*, Vol. 48, No. 3, 2011, pp. 777–785. https://doi.org/10.2514/1.C031022
[12] Stevenson, J. D., O'Young, S., and Rolland, L., "Estimated Levels of Safety for Small Unmanned Aerial Vehicles and Risk Mitigation Strategies," *Journal of Unmanned Vehicle Systems*, Vol. 3, No. 4, 2015, pp. 205–221. https://doi.org/10.1139/juvs-2014-0016
[13] Clothier, R., Walker, R., Fulton, N., and Campbell, D., "A Casualty Risk Analysis for Unmanned Aerial System (UAS) Operations over Inhabited Areas," *2nd Australasian Unmanned Air Vehicle Conference*, Australian International Aerospace Congress, 2007, pp. 1–15.
[14] Rudnick-Cohen, E., Herrmann, J. W., and Azarm, S., "Risk-Based Path Planning Optimization Methods for Unmanned Aerial Vehicles over Inhabited Areas," *Journal of Computing and Information Science in Engineering*, Vol. 16, No. 2, June 2016, Paper 13.
[15] Washington, A., Clothier, R. A., and Silva, J., "A Review of Unmanned Aircraft System Ground Risk Models," *Progress in Aerospace Sciences*, Vol. 95, Nov. 2017, pp. 24–44. https://doi.org/10.1016/j.paerosci.2017.10.00
[16] Coombes, M., Chen, W.-H., and Render, P., "Reachability Analysis of Landing Sites for Forced Landing of a UAS," *Journal of Intelligent and Robotic Systems*, Vol. 73, Nos. 1–4, 2014, pp. 635–653. https://doi.org/10.1007/s10846-013-9920-9
[17] Bradley, N., and Burke, D., "Potential Crash Location (PCL) Model," U.S. Naval Air Warfare Center Aircraft Div. NAWCADPAX/TR-2012/195, Patuxent River, MD, 2012.
[18] Atkins, E. M., Portillo, I. A., and Strube, M. J., "Emergency Flight Planning Applied to Total Loss of Thrust," *Journal of Aircraft*, Vol. 43, No. 4, 2006, pp. 1205–1216. https://doi.org/10.2514/1.18816
[19] Di Donato, P. F., and Atkins, E. M., "Evaluating Risk to People and Property for Aircraft Emergency Landing Planning," *Journal of Aerospace Information Systems*, Vol. 14, No. 5, 2017, pp. 259–278. https://doi.org/10.2514/1.I010513
[20] Barr, L., Newman, R., Ancel, E., Belcastro, C., Foster, J., Evans, J., and Klyde, D., "Preliminary Risk Assessment for Small Unmanned Aircraft Systems," *17th AIAA Aviation Technology, Integration, and Operations Conference*, AIAA Paper 2017-3272, 2017.
[21] Mennis, J., "Dasymetric Mapping for Estimating Population in Small Areas," *Geography Compass*, Vol. 3, No. 2, 2009, pp. 727–745. https://doi.org/10.1111/j.1749-8198.2009.00220.x
[22] Ratcliffe, M. R., "Providing Context and Meaning to Statistical Data: The Work of Census Bureau Geographers," *Geography Teacher*, Vol. 16, No. 3, 2019, pp. 107–111. https://doi.org/10.1080/19338341.2019.1619609
[23] Bhaduri, B., Bright, E., Coleman, P., and Urban, M. L., "LandScan USA: A High-Resolution Geospatial and Temporal Modeling Approach for Population Distribution and Dynamics," *GeoJournal*, Vol. 69, Nos. 1–2, 2007, pp. 103–117. https://doi.org/10.1007/s10708-007-9105-9
[24] Xia, C., Nie, G., Fan, X., and Zhou, J., "Research on the Estimation of the Real-Time Population in an Earthquake Area Based on Phone Signals: A Case Study of the Jiuzhaigou Earthquake," *Earth Science Informatics*, Vol. 13, No. 1, 2020, pp. 83–96. https://doi.org/10.1007/s12145-019-00418-8
[25] Li, X., Rowley, R., Kostelnick, J., Braaten, D., Meisel, J., and Hulbutta, K., "GIS Analysis of Global Impacts from Sea Level Rise," *Photogrammetric Engineering and Remote Sensing*, Vol. 75, No. 7, 2009, pp. 807–818. https://doi.org/10.14358/PERS.75.7.807
[26] Sutton, P., Elvidge, C., and Obremski, T., "Building and Evaluating Models to Estimate Ambient Population Density," *Photogrammetric Engineering and Remote Sensing*, Vol. 69, No. 5, 2003, pp. 545–553. https://doi.org/10.14358/PERS.69.5.545
[27] Linard, C., and Tatem, A. J., "Large-Scale Spatial Population Databases in Infectious Disease Research," *International Journal of Health Geographics*, Vol. 11, No. 1, 2012, Paper 7. https://doi.org/10.1186/1476-072X-11-7
[28] Poissant, A., Castano, L., and Xu, H., "Ground Impact and Hazard Mitigation for Safer UAV Flight Response," *International Conference on Unmanned Aircraft Systems*, IEEE, New York, 2018, pp. 1075–1084. https://doi.org/10.1109/ICUAS.2018.8453328
[29] Bogdiukiewicz, C., Butler, M., Hoang, T. S., Paxton, M., Snook, J., Waldron, X., and Wilkinson, T., "Formal Development of Policing Functions for Intelligent Systems," *2017 IEEE 28th International Symposium on Software Reliability Engineering (ISSRE)*, Inst. of Electrical and Electronics Engineers, New York, 2017, pp. 194–204.
[30] Verhaegen, M., Kanev, S., Hallouzi, R., Jones, C., Maciejowski, J., and Smail, H., "Fault Tolerant Flight Control—A Survey," Fault Tolerant Flight Control, Springer, Berlin, 2010, pp. 47–89.
[31] Azam, M., Pattipati, K., Allanach, J., Poll, S., and Patterson-Hine, A., "In-Flight Detection and Isolation in Aircraft Flight Control Systems," *2005 IEEE Aerospace Conference*, IEEE Publ., Piscataway, NJ, March 2005, pp. 3555–3565.
[32] Irving, F., *The Paths of Soaring Flight*, World Scientific, Singapore, 1999, pp. 17–31.
[33] Di Donato, P. F., and Atkins, E. M., "Optimizing Steady Turns for Gliding Trajectories," *Journal of Guidance, Control, and Dynamics*, Vol. 39, No. 12, 2016, pp. 2627–2637. https://doi.org/10.2514/1.G000319
[34] Jett, B., "The Feasibility of Turnback from a Low Altitude Engine Failure During the Takeoff Climb-Out Phase," *20th Aerospace Sciences Meeting*, AIAA Paper 1982-0406, 1982.
[35] Rogers, D. F., "Possible 'Impossible' Turn," *Journal of Aircraft*, Vol. 32, No. 2, 1995, pp. 392–397. https://doi.org/10.2514/3.46728.
[36] Anderson, J. D., *Fundamentals of Aerodynamics*, McGraw–Hill, New York, 1984, pp. 12–28.
[37] Yechout, T. R., *Introduction to Aircraft Flight Mechanics*, AIAA, Reston, VA, 2003, pp. 35–42.
[38] "Statistical Summary of Commercial Jet Airplane Accidents: Worldwide Operations, 1959–2018," 50th ed., Boeing Company, Chicago, IL, Sept. 2019, http://www.boeing.com/resources/boeingdotcom/company/about_bca/pdf/statsum.pdf [retrieved 12 March 2020].
[39] Wolf, S. E., "Modeling Small Unmanned Aerial System Mishaps Using Logistic Regression and Artificial Neural Networks," Thesis, U.S. Air Force Inst. of Technology, DTIC Accession Number ADA558464, Wright–Patterson AFB, OH, 2012.
[40] Sadraey, M. H., *Aircraft Performance: An Engineering Approach*, CRC Press, Boca Raton, FL, 2017, pp. 349–353.

E. Atkins
Associate Editor